Design of Silicon Nitride Based TE-Pass Polarizer at 850 nm for Integrated Fiber Optic Gyroscope

Zhiyu Guo, Ningfang Song, Linghai Kong, Jing Jin, and Zuchen Zhang

***Abstract*—In recent years, the rapid development of integrated optics provides a novel approach to realize miniaturized and lightweight fiber optic gyroscope (FOG). This paper proposes a TE-pass polarizer based on the silicon nitride on insulator (SNOI) platform operating at 850 nm, whose insertion loss is lower than 1.02 dB with the polarization extinction ratio (PER) larger than 47 dB. The proposed polarizer could directly edge-couple to the thin film lithium niobate (TFLN) modulator with a negligible loss (<0.19 dB) to form a combined hybrid modulator, which integrates the function of modulating, splitting, and polarizing. Compared with the traditional bulk lithium niobate modulator, the utilization of the hybrid modulator in FOGs could increase the optical power entering the fiber coil by 68% at 850 nm, which greatly facilitates the improvement of FOG precision. Furthermore, the undesired residual intensity modulation effect in the bulk lithium niobate modulator is also theoretically avoided by employing the hybrid modulator.**

***Index Terms*—Integrated optics, fiber optic gyroscope, TE-pass polarizer.**

I. Introduction

NOWADAYS, profit by the rapid development of integrated optics, the research on the miniaturized fiber optic gyroscope (FOG) has advanced to a new stage [1]. The on-chip integration of the discrete components in FOGs have been widely reported, including the on-chip laser source [2], the waveguide coils [3], [4], the integrated coupler chip [5], [6], and the multiple-quantum-well phase modulator [7]. Moreover, based on the multi-device integration, the optical transceiver module [8], [9] and the chip-scale integrated optical driver (IOD) [10] for FOG application are also proposed, stepping towards the full integration of the FOG. Among these researches, the integration of modulators is always of great interest, which is due to its determining effect on the FOG performance. Recently, the breakthrough research on the thin film lithium niobate (TFLN) modulator has been widely reported [11], [12]. Cheng Wang et al. design and fabricate the TFLN modulator, realizing 100 GHz bandwidth and 4.4 V half-wave voltage within a 5 mm-length TFLN modulator [13]. Based on the hybrid integration platform of the TFLN and silicon, a low-loss vertical coupling structure is brought in a 3 mm-length TFLN modulator, which performs >70 GHz bandwidth and 7.4 V half-wave voltage [14]. Through the introduction of the micro-structured electrodes, P. Kharel et al. achieve the 50 GHz bandwidth and 1.35 V half-wave voltage in a 20 mm-length modulator simultaneously [15]. Because of the excellent electro-optical properties and low-power consumption, TFLN has become an ideal material for next-generation modulators in integrated FOGs.

However, the currently proposed TFLN modulators could not be singly used in the integrated FOG. Typically, in the high-performance FOG, a polarizer with high polarization extinction ratio (PER) is significant for suppressing the polarization-related error in the fiber coil. In the traditional FOG, the bulk lithium niobate modulator not only modulates the propagating light, but also performs as the beam splitter and polarizer [16]. The bulk lithium niobate modulator consists of a Y-branch waveguide, which could split the beam and then guide it into the followed fiber coil. Besides, the Y-branch waveguide is fabricated by the annealed proton exchange process, where only the TE mode is supported [17], [18]. When the fundamental mode is launched into the bulk lithium niobate modulator, the TE mode could propagate stably in the waveguide, but the TM mode could not be confined within the waveguide and would leak into the substrate, resulting in the light polarizing naturally, as shown in Fig. 1. Nevertheless, since the different fabrication process, the TE mode and TM mode are both strongly confined in the TFLN waveguide, so a polarizer design is necessary when the TFLN modulator is used in the integrated FOG. However, the etching process for lithium niobate still faces many difficulties including the waveguide sidewall angles (generally 60∼80°), and it is challenging to realize dense and complex patterns on this platform. Therefore, considering the material similarity in the refractive index and transparency window, a polarizer design based on the silicon nitride (Si_3N_4) platform is proposed in this paper [19], [20].

The proposed TE-pass polarizer could directly edge couple to the TFLN modulator with a negligible coupling loss to form a hybrid modulator, which integrates the function of modulating, splitting, and polarizing. Compared to the bulk lithium niobate modulator widely used in the current FOG, the hybrid modulator redirects the TM mode that should have leaked into the substrate, improving the optical power entering the fiber coil by 68% at the wavelength of 850 nm, which benefits the improvement of FOG precision. Furthermore, due to the redirection rather than scattering of the TM mode (as illustrated in Fig. 1(b)), the undesired

Manuscript received 17 June 2024; revised 31 July 2024; accepted 2 August 2024. Date of publication 6 August 2024; date of current version 15 August 2024. *(Corresponding author: Zuchen Zhang.)*

Zhiyu Guo, Ningfang Song, Jing Jin, and Zuchen Zhang are with the School of Instrumentation and Optoelectronic Engineering, Beihang University, Beijing 100191, China (e-mail: zuchenzhang@buaa.edu.cn).

Linghai Kong is with the Beijing Institute of Control and Electronic Technology, Beijing 100038, China.

Digital Object Identifier 10.1109/JPHOT.2024.3439349

© 2024 The Authors. This work is licensed under a Creative Commons Attribution 4.0 License. For more information, see https://creativecommons.org/licenses/by/4.0/

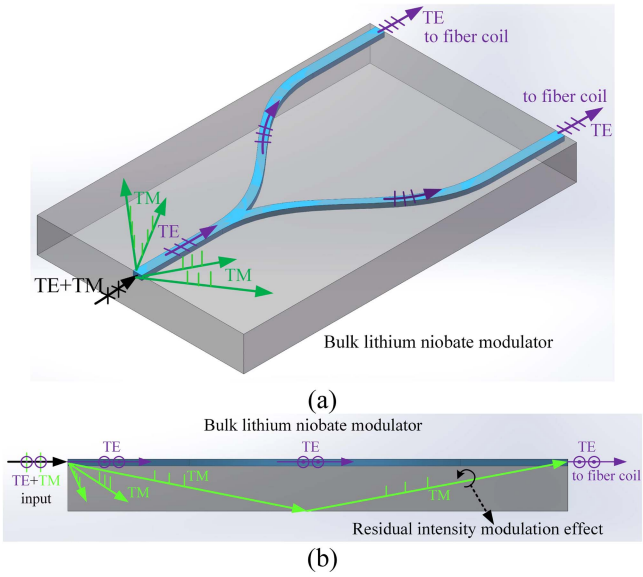

Fig. 1. The 3D diagram (a) and side view (b) of the beam propagation in the traditional bulk lithium niobate used in the FOG.

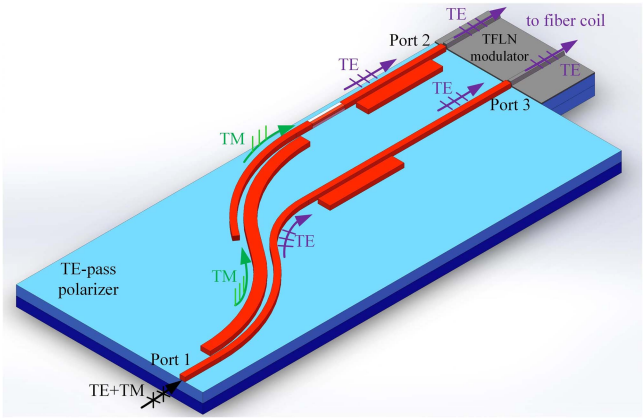

Fig. 2. The diagram of the TE-pass polarizer edge-coupling to the thin film lithium niobate (TFLN) modulator.

residual intensity modulation effect in the bulk lithium niobate modulator would not exist in the hybrid modulator theoretically [21]. This paper provides an easily implemented approach to realize on-chip light polarizing, which is also compatible with the TFLN modulator, paving the way for the application of TFLN modulator in the integrated FOG.

II. Polarizer Design and Optimization

The schematic diagram of the TE-pass polarizer is presented in Fig. 2, which is composed of two components: the polarization beam splitter (PBS) and the polarization rotator (PR). The mode launched from Port 1 is first split into the TM mode and TE mode by the PBS, which subsequently enter two separate channels. The TM mode would first propagate through the PR and be rotated by 90°, converting into the TE mode. Then the rotated-obtained TE mode would pass a directional coupler and arrive at Port 2. In the directional coupler, the residual TM mode

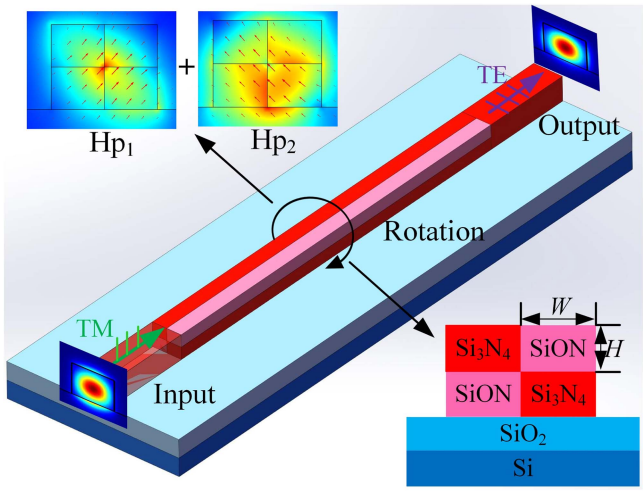

Fig. 3. The diagram of the polarization rotator (PR).

would be filtered out to improve the polarization extinction ratio (PER) of the device. Meanwhile, the TE mode early split by the PBS would also experience the filter process for purification and then arrive at Port 3. Finally, two TE mode beams with ultra-high PER are obtained and prepared to be launched into the TFLN modulator. After the low-loss edge coupling to the TFLN waveguide, the beams enter the TFLN modulator for further modulation and finally inject into the fiber coils.

In the following design, the 3-D eigenmode expansion (EME) algorithm and finite-difference time-domain (FDTD) method are utilized to optimize the structural parameters. Besides, considering the accuracy of FOG is inversely proportional to the operating wavelength, the proposed polarizer is optimized centered on 850 nm wavelength, which is the ideal operating wavelength for the miniaturized FOG [7].

A. Polarization Rotator (PR)

The polarization rotator (PR) is the core component of the proposed polarizer, which rotates the TM mode to the TE mode. Moreover, the PR shows more sensitivity to the structure based on our early research, so this paper starts with the design of the PR, and then accordingly determines the other waveguide dimension. Fig. 3 presents the proposed PR structure, which is composed of three parts: the input part, the rotation part, and the output part. The input and output part are Si_3N_4 waveguide with identical dimensions, supporting both TE and TM mode. The rotation part is a hybrid material waveguide composed of Si_3N_4 and SiON. The SiON is an emerging choice for integrated optics with the advantages of flexible refractive index, which could vary from the 1.45 of SiO_2 to 1.99 of Si_3N_4 by controlling the element proportion of oxygen and nitrogen during fabrication [22]. In the proposed design, the refractive index of SiON is set as 1.60 at 850 nm [23], while the refractive index of Si_3N_4 is 1.99 at 850 nm. As Fig. 3 presents, the hybrid waveguide is composed of four rectangular waveguides based on the Si_3N_4 and SiON with the same width and height denoted as W and H. Due to the centrosymmetric distribution of the hybrid waveguide, it could

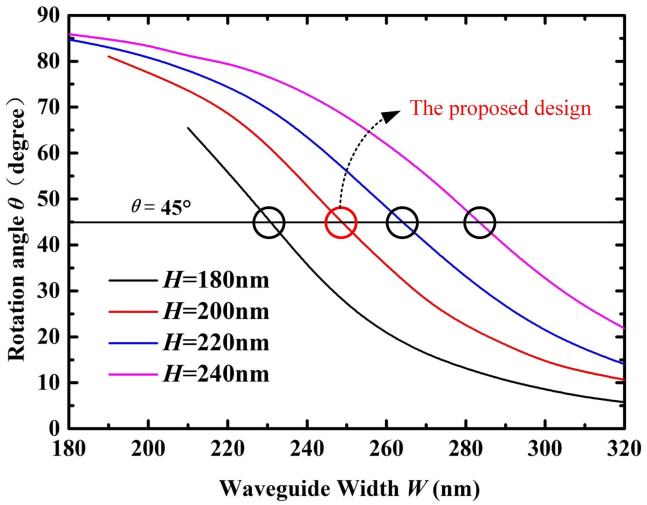

Fig. 4. The variation of rotation angle θ with the waveguide width W and waveguide height H.

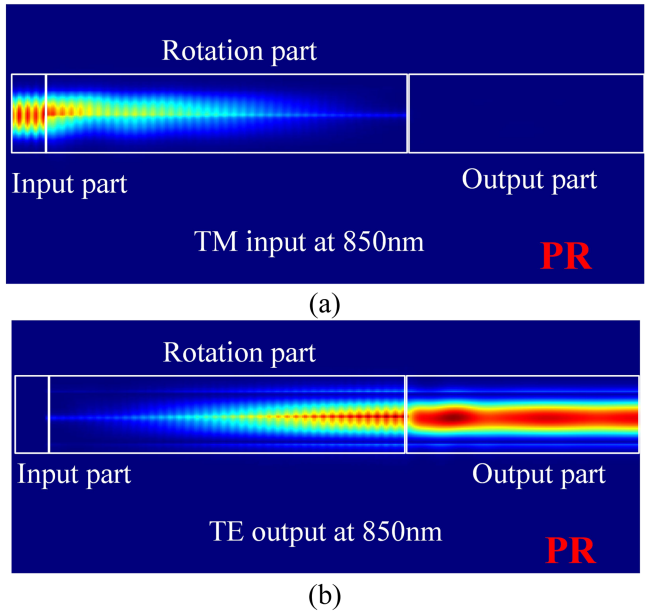

Fig. 5. The beam propagation in the PR for TM mode (a) and TE mode (b).

support two hybrid modes (Hp_1 and Hp_2) whose optical axes are rotated by 45° with respect to the x and y axes. When the TM mode is launched into the hybrid waveguide, the Hp_1 and Hp_2 modes would be excited and propagate with different propagation constants, β_1 and β_2 respectively. Therefore, a πrad phase difference between the two hybrid modes would be accumulated after the beam propagates for a half-beat length $L_\pi = \frac{\pi}{\beta_1 - \beta_2}$, resulting in the rotation of the TM mode by 90°. Accordingly, the TM mode is rotated into the TE mode, and the length of the rotation part equals to the half-beat length L_π of the two hybrid modes.

The rotation angle θ of the optical axis induced by the hybrid waveguide is defined as [24]

$$tan\,(\theta) = \iint \frac{n\,(x,y)\cdot E_x^2\,(x,y)\,dxdy}{n\,(x,y)\cdot E_y^2\,(x,y)\,dxdy}$$

where $n(x,y)$ is the refractive index distribution of the waveguide, and $E_x(x,y)$ and $E_y(x,y)$ are the transverse and horizontal electrical components of the hybrid mode, respectively. The variation of θ with the waveguide width W and height H is calculated, as demonstrated in Fig. 4. It can be concluded that for a constant waveguide height H, the rotation angle θ is inversely proportional to the waveguide width W. The parameter groups which make θ equal to 45° are all marked with circles in Fig. 4. When selecting the optimal parameter group, an overly small waveguide would lead to an increased difficulty for fabrication. Meanwhile, the waveguide dimension should not be too large to prevent the exciting of the higher order modes not only in the hybrid waveguide but also in the input/output Si_3N_4 waveguide. After taking these factors into consideration, the width W and height H of the rectangular waveguide are selected as 250 nm and 200 nm, respectively. Therefore, the width and height of the whole hybrid waveguide is $2W$ and $2H$, i.e., 500 nm and 400 nm. Based on this parameter group, the half-beat length L_π of the two hybrid modes is correspondingly calculated as 11 μm, which is also the length of the rotation part.

Here, it is worth mentioning that the fundamental mode in the proposed rectangular Si_3N_4 waveguide does not exist as the pure TE or TM mode, but presents as the quasi-TE or quasi-TM mode. By employing the Finite-Difference Eigenmode (FDE) solver, the quasi-TE and quasi-TM mode are calculated, whose TE polarization fractions are deduced as larger than 99% and lower than 1%, respectively. Besides, the refractive index difference between them is also obtained as about 0.016. For clarification, in this paper, the mentioned TE and TM mode confined within the rectangular waveguide all refer to the quasi-TE and quasi-TM mode, respectively.

Fig. 5 presents the beam propagation in the proposed PR when the TM mode is launched. The electric field intensity of the TM mode gradually decreases along the rotation part while that of the TE mode increases, demonstrating the conversion from the TM mode to the TE mode. The performance of the PR is evaluated by the polarization extinction ratio (PER) and insertion loss (IL), which are defined as [25]

$$\mathrm{PER} = 10\,\lg\left(\frac{P_{TE}}{P_{TM}}\right)$$

$$\mathrm{IL} = -10\,\lg\left(\frac{P_o}{P_i}\right)$$

where P_{TM} and P_{TE} correspondingly represent the output power of the TM mode and TE mode at the output end of the PR, P_o and P_i are the total output and the input power of the PR, respectively. The SLD source for FOG application operating at 850 nm typically has a bandwidth of 30 nm [26], so the wavelength sensitivity of PR is taken into discussion in a larger range of 850 $\pm$ 75 nm, fully covering the operating bandwidth of the SLD source. Fig. 6 illustrates that the PER of the PR reaches the maximum of 29 dB at 850 nm and keeps a level beyond 22 dB within the bandwidth of 850 nm$\pm$15 nm. The variation of

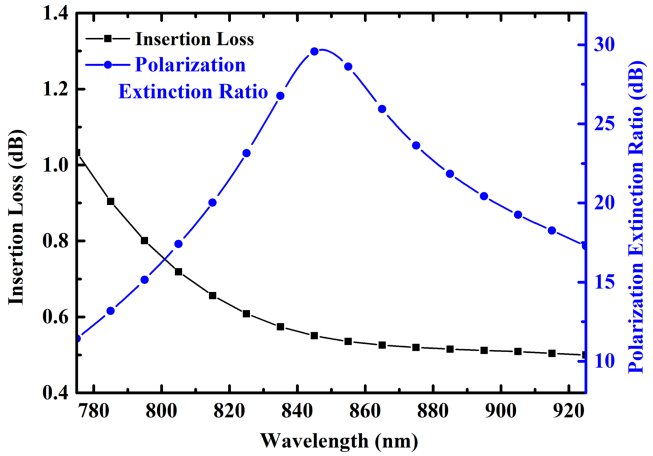

Fig. 6. The performance of PR with the operating wavelength.

PER with the wavelength implies the wavelength dependence of the PR, which results from the relevance between the half-beat length L_π and the operating wavelength. Meanwhile, the IL of the PR is less than 0.7 dB within the range of 850 nm $\pm$ 15 nm, which is mainly caused by the coupling loss at the facet between the hybrid waveguide and the input/output Si_3N_4 waveguide. Due to the different mode field distribution of the hybrid mode Hp_i (i = 1,2) and traditional TM/TE mode, an undesired coupling loss would be introduced at the coupling facet, which is a parasitic effect in this design [27].

B. Polarization Beam Splitter (PBS)

The PBS splits the fundamental mode into the TE mode and TM mode, which significantly determines the PER of the whole polarizer. Typically, in the formation of a high-performance FOG, a polarizer with the PER around 50 dB is necessary [28], [29]. Therefore, although many novel structures for PBS with ultra-small footprint have been proposed, the directional coupler (DC) structure is still employed in the proposed design because of the attractive properties of high PER and low fabrication challenge. As illustrated in Fig. 7, the proposed PBS is composed of three independent DCs denoted as DC_1, DC_2, and DC_3. The TM and TE mode launched from the input port are first split within the DC_1, and then enter the DC_2 and DC_3, respectively. The TM mode would couple again in the DC_2 and emit at the cross-port, which would be joint with the PR. Simultaneously, to improve the PER of the TE polarization, the TE mode passes the DC_3 performing as a TM mode filter, where the residual TM mode would be guided out without arriving at the through-port. Accordingly, the TM and TE mode are split and emit from the cross-port and through-port of the PBS respectively. Given that the DC_3 only performs as a mode filter and has little influence for the mode splitting, the PBS design starts with DC_1 and DC_2.

In the design of DC_1 and DC_2, the width (W_1, W_2) and central angle α of the bent waveguide are optimized to meet the phase-matching condition for TM mode only, i.e., $n_{eff1} \cdot R_1 = n_{eff2} \cdot R_2$, where n_{eff1} and n_{eff2} are the refractive indices of the TM mode in the two bent waveguides [30]. For the TE mode, a large

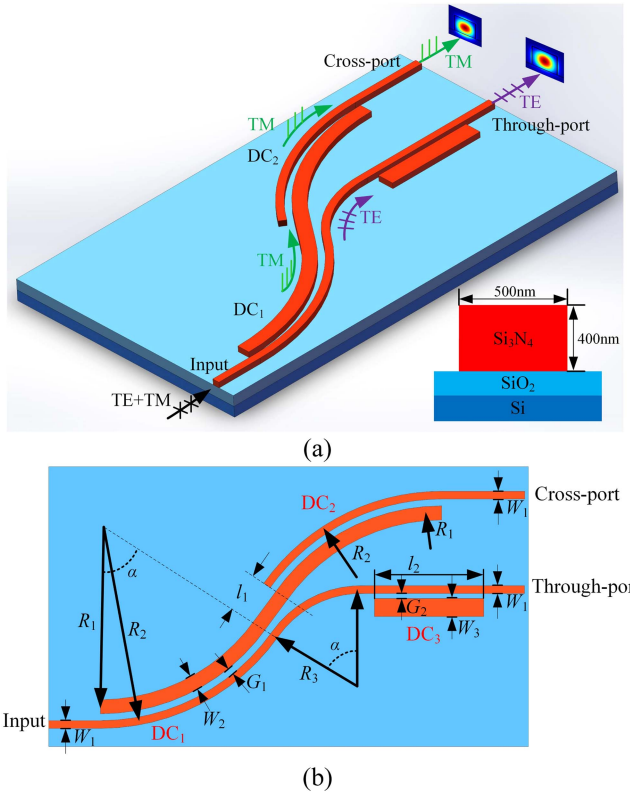

Fig. 7. The 3D diagram (a) and top view (b) of the polarization beam splitter (PBS).

phase mismatch is necessary for the weak cross coupling. It has been reported that, to realize the low loss propagation in the bent Si_3N_4 waveguide, the bending radius is preferably larger than 20 μm [31]. Therefore, considering both the low bending loss and large phase mismatch for the TE mode, the bending radius R_1 and R_2 of the bent waveguide are chosen as 25 μm and 25.75 μm, respectively. Fig. 8 shows the calculated $n_{eff1} \cdot R_1$ and $n_{eff2} \cdot R_2$ of the bent waveguide varying with the waveguide width. For the convenience of easy connection with the PR, the waveguide width W_1 and height H_1 of the input and output waveguide are correspondingly set as 500 nm and 400 nm, which is identical to that of the PR. Accordingly, the waveguide width W_2 is determined as 719 nm to fulfil the phase-matching condition for TM mode, while a large phase mismatch is conducted for the TE mode at the same time. Based on the above parameters, the gap G_1 between the two bent waveguides is about 140 nm, which could be realized regarding the electron beam lithography process. Besides, to spatially separate the TM and TE mode which has been split by the DC_1, a straight waveguide l_1 with the length of 3 μm is introduced to connect the DC_1 and DC_2, guiding the TM mode into DC_2. Meanwhile, the TE mode is guided by a bent waveguide R_3 with a bending radius of 20 μm into the DC_3.

The effect of the central angle α of the bent waveguide on the transmissions are discussed separately for TE and TM mode without DC_3, as Fig. 9 depicts. It can be seen that due to the phase mismatch between the two bent waveguides, the transmission for TE mode is insensitive to the central angle α. However, for the

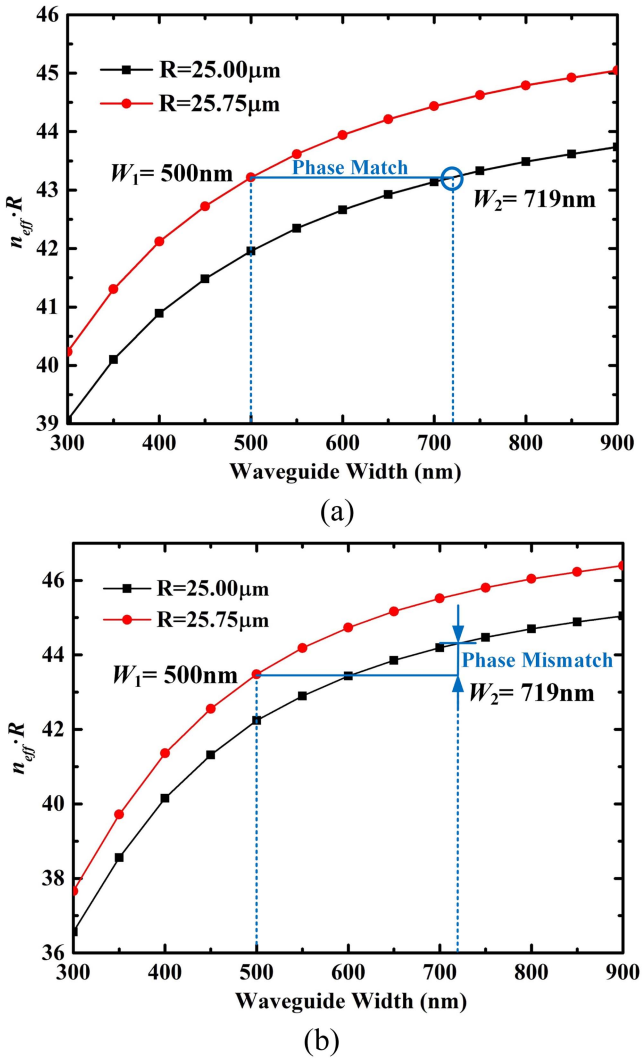

Fig. 8. Calculated n_{eff}·R of the two bent waveguides for (a) TM mode and (b)TE mode.

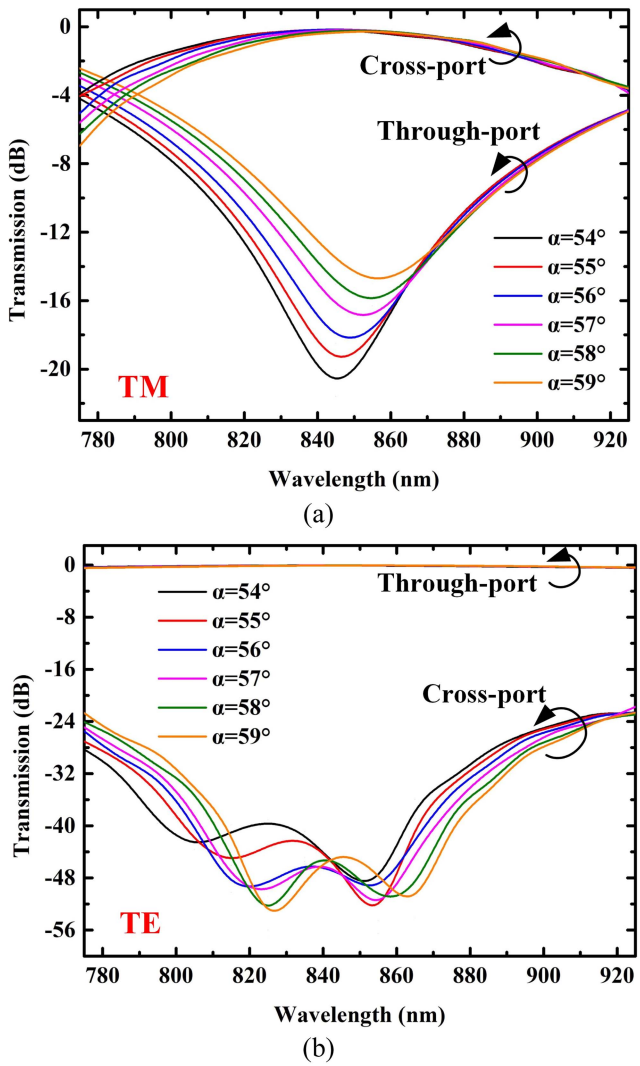

Fig. 9. Transmissions of the PBS without DC_3 at different central angle α. (a) TM mode; (b) TE mode.

TM mode, the center wavelength of the transmission experiences a gentle shift as the central angle α increases from 54° to 58°, which is caused by the wavelength dependence of the evanescent coupling [32]. To stabilize the center wavelength at 850 nm, the central angle α of the bent waveguide is chosen as 55°.

To further improve the PER for TE polarization, the DC_3 is introduced to filter out the residual TM mode emitting from the through-port. Similarly, in the design of DC_3, a straight waveguide with 400 nm height is employed to create the phase-matching condition for the TM mode only, simultaneously leading to a large mismatch for TE mode. It is found that when W_3 equals 1.172 μm, the TM_1 mode of the straight waveguide matches with the TM_0 mode of the output waveguide of the PBS, while the TE mode of the output waveguide performs a mismatch with any guided mode in the straight waveguide. The gap G_2 between the straight waveguide and the output waveguide is optimized as 150 nm considering both the insertion loss and fabrication difficulty. Fig. 10 shows the transmission of the TE and TM mode when the DC_3 is cascaded at the through-port as the coupling length l_2 varies from 23 μm to 28 μm. It can be concluded that the introduction of the DC_3 has little influence on the transmissions at the cross-port for both TE and TM mode. At the trough-port, because of the large mismatch for the TE mode, the extra loss resulting from the cross coupling in the DC_3 could also be neglected. However, the TM mode at the trough-port is effectively depressed by the DC_3, which presents a 35 dB decrease in transmission at 850 nm compared with that without the DC_3. Finally, when selecting the optimal coupling length $l_2 = 26$ μm, the PER of the PBS achieves the maximum of 53 dB for TM mode and 52 dB for TE mode at 850 nm, and maintains beyond 34 dB for TM mode and 35 dB for TE mode in the range of 850 nm±15 nm. Fig. 11 illustrates the beam propagation of the TM and TE mode in the proposed PBS at the wavelength of 850 nm.

C. TE-Pass Polarizer

The TE-pass polarizer is cascaded by the PBS and PR. Due to the uniform design of the waveguide dimension

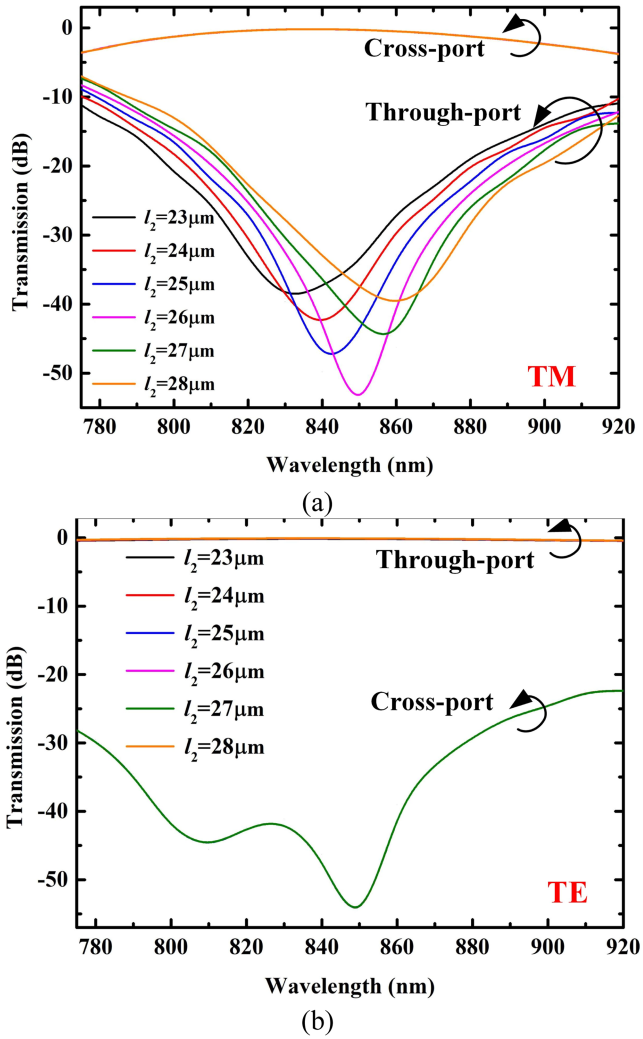

Fig. 10. Transmissions of the PBS with DC_3 at different coupling length l_2. (a) TM mode; (b) TE mode.

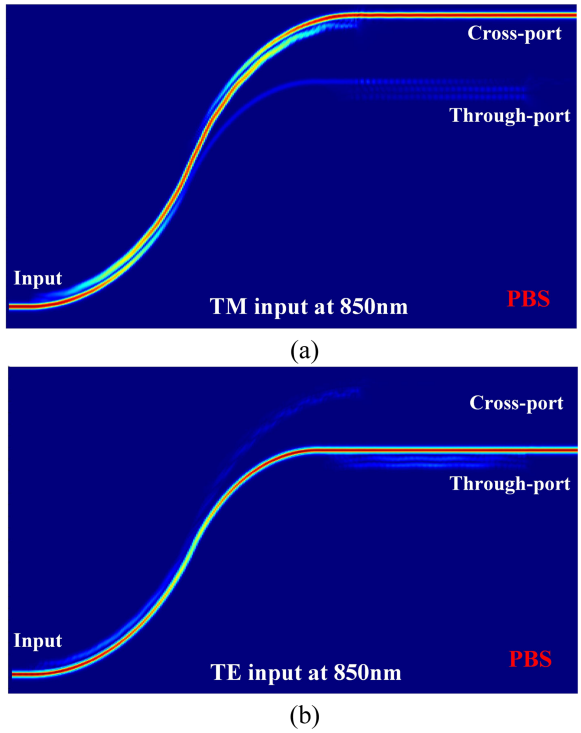

Fig. 11. Beam propagation in the PBS. (a)TM mode (b) TE mode.

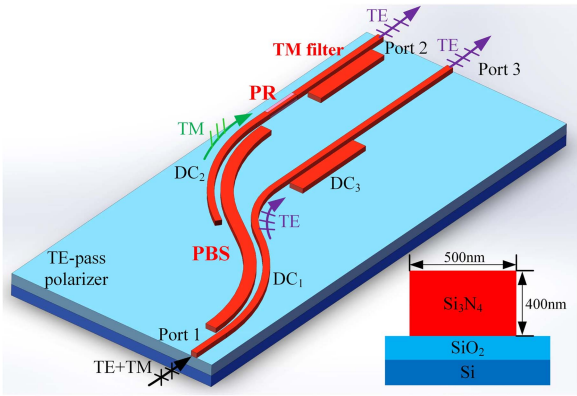

Fig. 12. The diagram of the TE-pass polarizer.

(500 nm × 400 nm), it is unnecessary to introduce any additional connection structure between the PBS and PR. In the proposed polarizer, the TM mode launched into Port 1 would pass the cross-port of the PBS and enter the PR, finally arrive at Port 2. In contrast, the TE mode launched into Port 1 would pass the through-port of the PBS and eventually reach Port 3. The performance of the cascade structure is accordingly discussed, and the result indicates that the PER for the TE mode outputting at Port 3 shows little difference with that of the through-port of the PBS. However, for the TE beam arriving at Port 2, the PER of the cascade structure only reaches ∼20 dB at 850 nm, which is ∼33 dB lower than that of the TM mode at the cross-port of the PBS. There are two main explanations. First, due to the limited conversion efficiency of the PR, the TM mode entering the PR could not be entirely conversed to the TE mode, decreasing the PER of the TE mode at Port 2. Second, the residual TE mode at the cross-port of the PBS would be rotated into the TM mode after passing through the PR, further degrading the PER of the TE mode at Port 2. To increase the PER of the TE mode at Port 2, a TM mode filter is added after the PR, whose structure is identical to the DC_3 used in the PBS. The whole structure of the proposed TE-pass polarizer is then obtained as Fig. 12 shows, which occupies a footprint of 86 μm × 24 μm.

Fig. 13 depicts the beam propagation in the proposed TE-pass polarizer when the TM and TE mode are individually launched into the device. The input TM mode split by the PBS enters the PR and is rotated into the TE mode, so the electric field intensity of the TM mode gradually weakens and is replaced by that of the TE mode during the propagation. In contrast, the input TE mode split by the PBS would almost completely pass the device and arrive at Port 3. The PER and IL of the TE-pass polarizer is calculated for Port 2 and Port 3 individually, as shown in Fig. 14. For the TE mode at the Port 3, the IL is 0.12 dB and the PER is

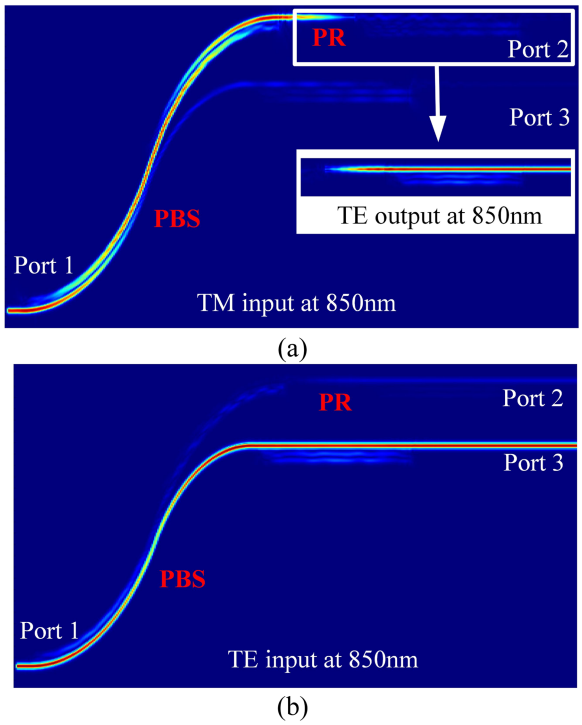

Fig. 13. The beam propagation in the TE-pass polarizer when the TM mode (a) or TE mode (b) is launched in Port 1.

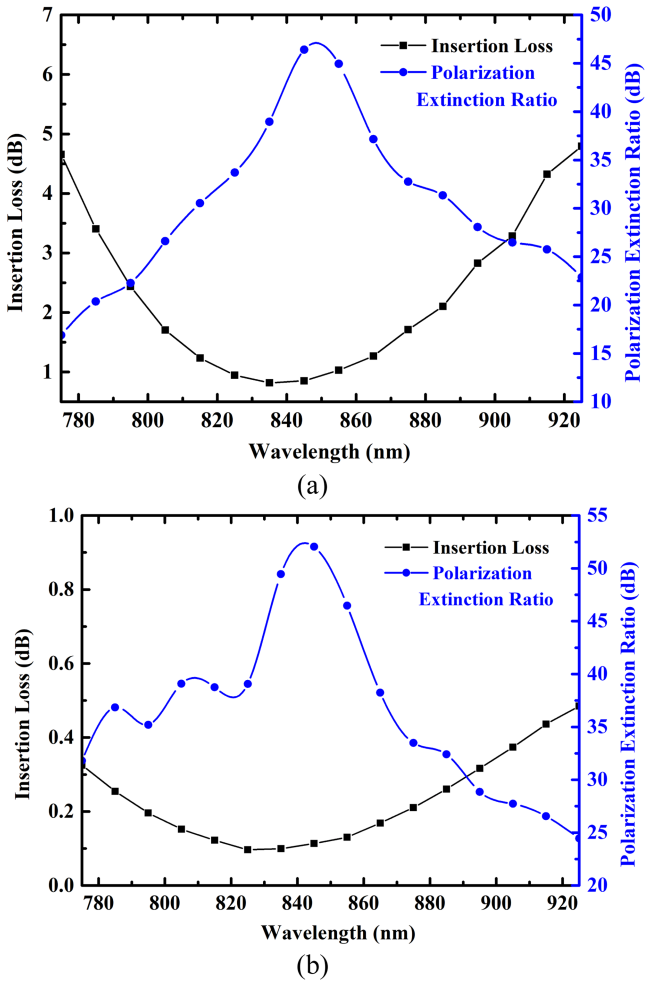

Fig. 14. The performance of the TE-pass polarizer at the Port 2 (a) and Port 3 (b).

52 dB at 850 nm, which keep lower than 0.2 dB and higher than 36 dB respectively within the wavelength of 850 nm ± 15 nm. However, for the TE mode at the Port 2, the IL is 1.02 dB and the PER is 47 dB at 850 nm, which keep lower than 1.26 dB and higher than 35 dB respectively from 835 nm to 865 nm. One reason for the higher IL at Port 2 is the cross-coupling of the TM mode in the PBS, resulting in the double of the cross-coupling loss. The other reason is that the introduction of the PR causes the undesired coupling loss at the facet between the waveguides with different materials, as discussed before.

D. Coupling Between the TE-Pass Polarizer and TFLN Modulator

Due to the similar refractive index and similar transparency window to the TFLN material, the Si_3N_4 has been considered as the ideal material for hybrid integration with the TFLN platform [19]. Here, the feasibility of direct edge coupling between the proposed polarizer and the TFLN modulator is discussed. As shown in Fig. 15, the separately manufactured TFLN and Si_3N_4 chips are high-precision aligned at the polished surfaces. After bonding to the polarizer, the TFLN modulator could integrate the function of light polarizing, and meet the demand for FOGs or other applications with polarization requirement. Besides, it should be claimed that the TE mode mentioned here also refers to the quasi-TE mode.

As Fig. 15 shows, the TFLN waveguide is edge-coupled to the output Si_3N_4 waveguide of the proposed polarizer. Given the fact that the practically etched TFLN waveguide presents a sidewall angle (generally 60∼80°), the TFLN waveguide model

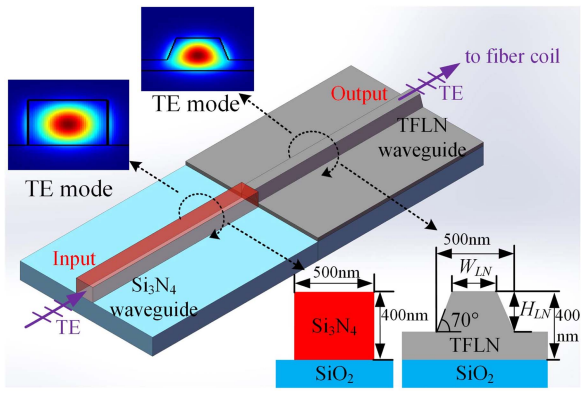

Fig. 15. The coupling between the Si_3N_4 waveguide and TFLN waveguide.

is set as a double-layer structure, including a planar film as the lower layer and a trapezoidal line waveguide as the upper layer. The trapezoidal line waveguide is obtained by the dry etching process, so the height of the trapezoidal waveguide H_{LN} is the etching depth on the TFLN wafer. In this paper, the sidewall angle of the TFLN waveguide is selected as 70°, which has

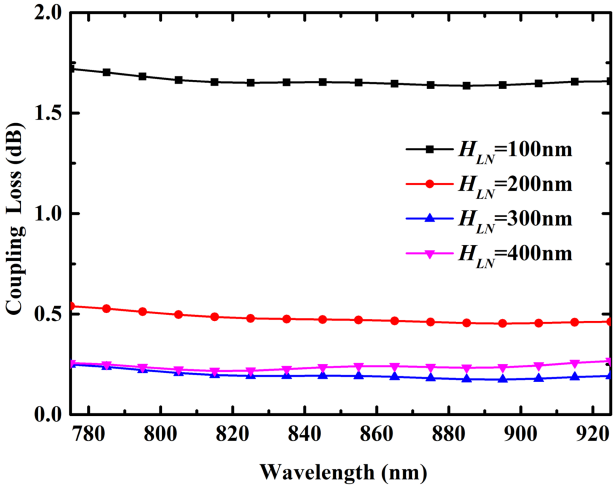

Fig. 16. Coupling loss between the Si_3N_4 waveguide and TFLN waveguide with etching depth H_{LN}.

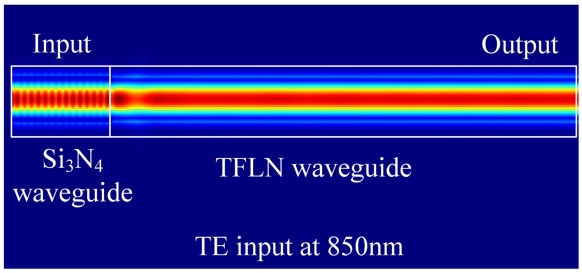

Fig. 17. The beam propagation from the Si_3N_4 waveguide to the TFLN waveguide.

been stably achieved and widely reported [27]. To minimize the coupling loss, the sum of the film thickness and trapezoidal waveguide height H_{LN} is fixed at 400 nm, which is identical to the height of the Si_3N_4 waveguide of the proposed polarizer. Accordingly, the bottom width of the trapezoidal waveguide is also set identically to the width of the Si_3N_4 waveguide, i.e., 500 nm. Thus, the top width of the trapezoidal waveguide W_{LN} is solely determined by the height H_{LN} ($W_{LN} = 500 - \frac{2 \cdot H_{LN}}{tan(70^0)}$), and the profile of the double-layer TFLN waveguide model is also accordingly determined.

Fig. 16 illustrates the variation of the transmission of the edge coupling model with the trapezoidal waveguide height H_{LN} (i.e., the etching depth on the TFLN wafer). It can be seen that the coupling loss between the Si_3N_4 waveguide and TFLN waveguide is insensitive to the operating wavelength but directly determined by the profile of the TFLN waveguide. As the etching depth H_{LN} increases from 100 nm to 400 nm, the coupling loss between the Si_3N_4 waveguide and TFLN waveguide decreases rapidly and then stabilizes at a fairly low level. After the simulation, the optimal etching depth H_{LN} is found as 300 nm, and the coupling loss between the Si_3N_4 waveguide and TFLN waveguide is calculated, which presents lower than 0.19 dB within the range of 850 nm$\pm$15 nm. Fig. 17 shows the beam propagation in the established edge-coupling model.

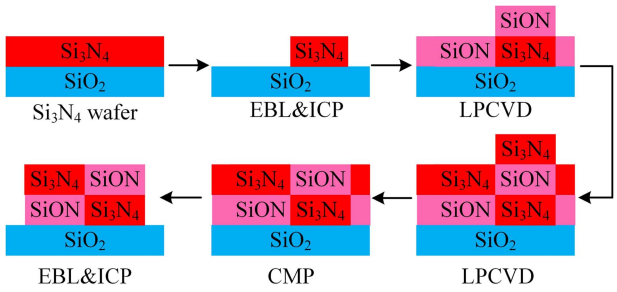

Fig. 18. The fabrication process designing for the proposed PR.

Thus, combing the coupling loss between the Si_3N_4 waveguide and TFLN waveguide, the total IL of the hybrid modulator composed of the TE-pass polarizer and the TFLN modulator could be calculated at 850 nm, which is 1.21 dB and 0.31 dB at Port 2 and Port 3, respectively. In the traditional bulk lithium niobate modulator, the TE mode could pass through but the TM mode would leak into the substrate, so only 50% of the input optical power is utilised for modulation and subsequently enters the fiber coil. However, in the proposed hybrid modulator, the TM mode would be redirected and then converted into the TE mode for modulation, finally entering the fiber coil. Therefore, taking into account the IL at Port 2 and Port 3, theoretically 84% of the input optical power is utilised in the proposed hybrid modulator, which is improved by 68%.

However, the coupling loss of the Si_3N_4 chip should also be taken into consideration when evaluating the performance of this design. In the traditional bulk device, the fundamental mode of the lithium niobate waveguide presents a comparable size with that of the fiber, and the coupling loss between them could be neglected. But in the design of Si_3N_4 waveguide, due to the mode mismatch, the coupling loss has become a complicated and common problem. Currently various designs on the spot size converters and grating couplers are reported, and the theoretical coupling loss between the Si_3N_4 chip and lensed fiber is reduced to 0.22 dB [33], [34]. Besides, based on the spot size converter, the coulpling between the integrated waveguide with the light source is also discussed, presenting a coupling loss of 0.63 dB [35], [36]. To realize the ideal performance in this design, more efforts should be made on the optimization of the chip coupling loss.

III. Feasibility and Tolerance of the Fabrication

The proposed TE-pass polarizer is composed of the PBS and PR, and by employing the electron beam lithography (EBL) process, the pattern of the PBS structure could be directly writing on the electron beam resist and then transferred on a Si_3N_4 wafer through the one-step inductively coupled plasma (ICP) etching process. However, the fabrication feasibility of the proposed PR remains to be discussed. Here, the fabrication process designing for the proposed PR is illustrated as shown in Fig. 18, mainly involving in the fabrication of the hybrid material (Si_3N_4 and SiON) waveguide.

Based on a silicon nitride on insulator (SNOI) chip, the Si_3N_4 waveguide at the bottom of the hybrid waveguide is first obtained

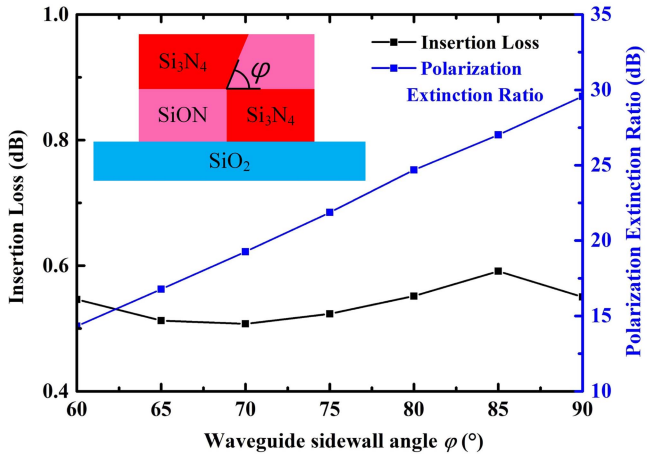

Fig. 19. The influence of the fabrication defect on the performance of the PR.

by the EBL&ICP process. Then, the 200 nm thickness SiON film is deposited on the obtained Si_3N_4 chip through the low pressure chemical vapor deposition (LPCVD) process. After adjusting the proportion of deposited gas, a 200 nm thickness Si_3N_4 film is continuously deposited on this chip, which followed by the chemical mechanical polishing (CMP) process on the chip surface. Finally, the hybrid waveguide is achieved utilizing the EBL&ICP process on the twice-deposited chip.

In this fabrication process, due to the existence of the difference in height, the deposited SiON waveguide above the etched Si_3N_4 waveguide might present a sidewall angle φ, as Fig. 19 depicts. Therefore, the influence of the sidewall angle φ on the PR performance is investigated. Fig. 19 presents that the defect of the waveguide sidewall has few influences on the IL of the PR, as it fluctuates within the range of less than 0.1 dB as the sidewall angle φ varies from 60° to 90°. However, the PER of the PR presents slight sensitivity to the sidewall angle φ, which drops from 29 dB to 15 dB as φ decreases from 90° to 60°. The defect of the waveguide sidewall would change the distribution of the hybrid modes Hp_1 and Hp_2, whose optical axes are no longer rotated by 45° with respect to the x and y axes. Thus, the conversion efficiency of the PR would be degraded, and the PER is accordingly decreased. However, when the sidewall angle φ exceeds 72°, the PER of the PR can still be higher than 20 dB at the wavelength of 850 nm. Furthermore, the residual TM mode that are not rotated into the TE mode would be filtered out by the TM filter before arriving at the Port 2 of the polarizer. Therefore, the PER degradation of the PR induced by the sidewall defect has little impact on the performance of the whole TE-pass polarizer.

IV. Conclusion

This paper proposes a TE-pass polarizer based on the SNOI platform operating at 850 nm, which is composed of the PBS and PR, occupying the footprint of 86 μm × 24 μm. The fundamental mode injected into the polarizer would first be split into the TM and TE mode by the PBS, and the TM mode would subsequently enter the PR to be rotated into the TE mode and emit from the Port 2 of the polarizer. In contrast, the TE mode split by the PBS would directly emit from the Port 3 of the polarizer. The simulation result shows that the IL of the polarizer is 1.02 dB and 0.12 dB at 850 nm at Port 2 and Port 3 respectively, while the PER is 47 dB and 52 dB respectively.

The proposed TE-pass polarizer could directly edge-couple to the TFLN modulator with a wavelength-insensitive coupling loss (<0.19 dB) to form a hybrid modulator, which integrates the function of modulating, splitting, and polarizing. Compared to the traditional bulk lithium niobate modulator, the utilization of the hybrid modulator in FOG could redirect the TM mode and thus improve the optical power entering the fiber coil by 68% at 850 nm, which benefits the improvement of FOG precision. Furthermore, the undesired residual intensity modulation effect in the bulk lithium niobate modulator is also theoretically avoided in the hybrid modulator. This paper bypasses the challenging etching process on the TFLN and designs a TE-pass polarizer compatible with the TFLN modulator, paving the way for applying TFLN modulators to integrated FOGs or other scenarios with polarization requirement.

References

[1] S. Srinivasan, R. Moreira, D. Blumenthal, and J. Bowers, "Design of integrated hybrid silicon waveguide optical gyroscope," *Opt. Exp.*, vol. 22, no. 21, pp. 24988–24993, Oct. 2014.
[2] T. Komljenovic, M. A. Tran, M. Belt, S. Gundavarapu, D. J. Blumenthal, and J. E. Bowers, "Frequency modulated lasers for interferometric optical gyroscopes," *Opt. Lett.*, vol. 41, no. 8, pp. 1773–1776, Apr. 2016.
[3] S. Gundavarapu et al., "Interferometric optical gyroscope based on an integrated Si_3N_4 low-loss waveguide coil," *J. Lightw. Technol.*, vol. 36, no. 4, pp. 1185–1191, Feb. 2018.
[4] B. B. Wu, Y. Yu, J. B. Xiong, and X. L. Zhang, "Silicon integrated interferometric optical gyroscope," *Sci. Rep.*, vol. 8, Jun. 2018, Art. no. 8766.
[5] L. Wang, D. R. Halstead, T. D. Monte, J. A. Khan, J. Brunner, and M. A. K. van Heyningen, "Low-cost, high-end tactical-grade fiber optic gyroscope based on photonic integrated circuit," in *Proc. IEEE Int. Symp. Inertial Sensors Syst.*, 2019, pp. 1–2.
[6] Z. Guo et al., "Three-axis interferometric fiber optic gyroscope with silica integrated coupler chip," *IEEE Sensors J.*, vol. 23, no. 9, pp. 9323–9332, May 2023.
[7] H. Ohe, H. Shimizu, and Y. Nakano, "InGaAlAs multiple-quantum-well optical phase modulators based on carrier depletion," *IEEE Photon. Technol. Lett.*, vol. 19, no. 22, pp. 1816–1818, Nov. 2007.
[8] K. Shang et al., "Ultra-small interferometric fiber optic gyroscope with an integrated optical chip," *Chin. Opt. Lett.*, vol. 20, no. 4, Jan. 2022, Art. no. 040601.
[9] K. Shang, M. Lei, Q. Xiang, Y. Na, and L. Zhang, "Tactical-grade interferometric fiber optic gyroscope based on an integrated optical chip," *Opt. Commun.*, vol. 485, Apr. 2021, Art. no. 126729.
[10] M. A. Tran, T. Komljenovic, J. C. Hulme, M. J. Kennedy, D. J. Blumenthal, and J. E. Bowers, "Integrated optical driver for interferometric optical gyroscopes," *Opt. Exp.*, vol. 25, no. 4, pp. 3826–3840, Feb. 2017.
[11] A. J. Mercante, P. Yao, S. Shi, G. Schneider, J. Murakowski, and D. W. Prather, "110 GHz CMOS compatible thin film $LiNbO_3$ modulator on silicon," *Opt. Exp.*, vol. 24, no. 14, pp. 15590–15595, Jul. 2016.
[12] C. Wang, M. Zhang, B. Stern, M. Lipson, and M. Lončar, "Nanophotonic lithium niobate electro-optic modulators," *Opt. Exp.*, vol. 26, no. 22, pp. 1547–1555, Jan. 2018.
[13] C. Wang et al., "Integrated lithium niobate electro-optic modulators operating at CMOS-compatible voltages," *Nature*, vol. 562, pp. 101–104, Sep. 2018.
[14] M. He et al., "High-performance hybrid silicon and lithium niobate Mach–Zehnder modulators for 100 Gbit s-1 and beyond," *Nature Photon.*, vol. 13, pp. 359–364, Mar. 2019.
[15] P. Kharel, C. Reimer, K. Luke, L. He, and M. Zhang, "Breaking voltage-bandwidth limits in integrated lithium niobate modulators using micro-structured electrodes," *Optica*, vol. 8, no. 3, pp. 357–363, Mar. 2021.
[16] H. C. Lefèvre, *Fiber Optic Gyroscope*. Norwood, MA, USA: Artech House, 2014.

[17] T. Findakly and M. Bramson, "High-performance integrated-optical chip for a broad range of fiber-optic gyro applications," *Opt. Lett.*, vol. 15, no. 12, pp. 673–675, Jun. 1990.
[18] L. M. Johnson, "Integrated-optical components for fiber gyroscopes," *Proc. SPIE*, vol. 566, pp. 96–98, 1986.
[19] X. Han et al., "Integrated subwavelength gratings on a lithium niobate on insulator platform for mode and polarization manipulation," *Laser Photon. Rev.*, vol. 16, no. 7, May 2022, Art. no. 2200130.
[20] S. Jin, L. Xu, H. Zhang, and Y. Li, "$LiNbO_3$ thin-film modulators using silicon nitride surface ridge waveguides," *IEEE Photon. Technol. Lett.*, vol. 28, no. 7, pp. 736–739, Apr. 2016.
[21] J. Liu, C. Zhang, Y. Zheng, J. Song, F. Gao, and D. Yang, "Suppression of nonlinear residual intensity modulation in multifunction integrated optic circuit for fiber-optic gyroscopes," *J. Lightw. Technol.*, vol. 38, no. 6, pp. 1572–1579, Mar. 2020.
[22] K. Nakayama, Y. Shoji, and T. Mizumoto, "Single trench SiON waveguide TE-TM mode converter," *IEEE Photon. Technol. Lett.*, vol. 24, no. 15, pp. 1310–1312, Aug. 2012.
[23] L. Zhu, M. Li, J. Ye, and J.-J. He, "Highly-sensitive optical waveguide sensor based on SiON using two cascaded-microring resonators," in *Proc. Asia Commun. Photon. Conf.*, 2013, pp. 1–3.
[24] L. Gao, Y. Huo, J. S. Harris, and Z. Zhou, "Ultra-compact and low-loss polarization rotator based on asymmetric hybrid plasmonic waveguide," *IEEE Photon. Technol. Lett.*, vol. 25, no. 21, pp. 2081–2084, Nov. 2013.
[25] F. Wang, Y. Chen, T. Ma, H. Liu, X. Wang, and C. Jin, "Mid-infrared polarization rotator based on a Si_3N_4-CaF_2 hybrid plasmonic waveguide with asymmetric metal claddings," *Appl. Opt.*, vol. 60, no. 8, pp. 2441–2449, Mar. 2021.
[26] H. Li, J. Zhang, Y. Qu, X. Gao, B. Bo, and G. Liu, "High-performance 850-nm superluminescent diodes," *Proc. SPIE*, vol. 6020, pp. 625–628, 2005.
[27] Y. Zhao et al., "Compact lithium-niobate-on-insulator polarization rotator based on asymmetric hybrid plasmonics waveguide," *IEEE Photon. J.*, vol. 13, no. 4, Aug. 2021, Art. no. 4800105.
[28] C. Laskoskie and W. Trammell, "Depolarized interferometric fiber-optic gyro with improved polarization error suppression," *Proc. SPIE*, vol. 1795, pp. 118–125, 1993.
[29] J. Liu, C. Zhang, F. Gao, J. Song, X. Xu, and Z. Guo, "Method for improving the polarization extinction ratio of multifunction integrated optic circuits," *Opt Exp.*, vol. 29, no. 18, pp. 28096–28103, Aug. 2021.
[30] D. Dai and J. E. Bowers, "Novel ultra-short and ultra-broadband polarization beam splitter based on a bent directional coupler," *Opt Exp.*, vol. 19, no. 19, pp. 18614–18620, Sep. 2011.
[31] J. H. Song, T. D. Kongnyuy, P. De Heyn, S. Lardenois, R. Jansen, and X. Rottenberg, "Low-loss waveguide bends by advanced shape for photonic integrated circuits," *J. Lightw. Technol.*, vol. 38, no. 12, pp. 3273–3279, Jun. 2020.
[32] H. Wu, Y. Tan, and D. Dai, "Ultra-broadband high-performance polarizing beam splitter on silicon," *Opt Exp.*, vol. 25, no. 6, pp. 6069–6075, Mar. 2017.
[33] Y. Zhang et al., "High-efficiency and compact polarization-insensitive multi-segment linear silicon nitride edge couple," *Photonics*, vol. 10, no. 5, Apr. 2023, Art. no. 510.
[34] V. Vitali, C. Lacava, T. D. Bucio, F. Y. Gardes, and P. Petropoulos, "Highly efficient dual-level grating couplers for silicon nitride photonics," *Sci. Rep.*, vol. 12, Sep. 2022, Art. no. 15436.
[35] L. Li, Y. Ma, Y. Zhang, S. Li, Y. Shi, and X. Chen, "Multi-tip edge coupler for integration of a distributed feedback semiconductor laser with a thin-film lithium niobate modulator," *Appl. Opt.*, vol. 60, no. 16, pp. 4814–4819, Jun. 2021.
[36] Y. Zhang et al., "Reconfigurable spot size converter for the silicon photonics integrated circuit," *Opt Exp.*, vol. 29, Oct. 2021, Art. no. 37703.